First measurements with a Coherence Imaging Charge Exchange Recombination Spectroscopy (CICERS) diagnostic at Wendelstein 7-X

OPEN ACCESS
IOP Publishing
Plasma Physics and Controlled Fusion
Plasma Phys. Control. Fusion **66** (2024) 045012 (11pp)
https://doi.org/10.1088/1361-6587/ad290e

First measurements with a Coherence Imaging Charge Exchange Recombination Spectroscopy (CICERS) diagnostic at Wendelstein 7-X

R Lopez-Cansino[1,*], V Perseo[2], E Viezzer[1], D M Kriete[3], O P Ford[2], T Romba[2], P Zs Poloskei[2] and the W7-X Team[4]

[1] Dept. of Atomic, Molecular and Nuclear Physics, University of Seville, Seville, Spain
[2] Max-Planck-Institut für Plasmaphysik, Greifswald, Germany
[3] Auburn University, Auburn, AL, United States of America

E-mail: rlopez1@us.es

Received 15 December 2023, revised 22 January 2024
Accepted for publication 13 February 2024
Published 1 March 2024

Abstract

In this work, the Coherence Imaging Spectroscopy technique is exploited for active charge exchange radiation measurements to infer high spatial resolution 2D ion temperature (T_i) maps in the core region of Wendelstein 7-X plasmas. A synthetic model of the diagnostic is developed and used for the optimization of the hardware components for the expected ion temperatures ($T_i \sim 2$ keV) prioritizing T_i measurements while also considering the ion velocity flow resolution. The experimental set-up is shown and the diagnostic calibration procedure for T_i measurements is introduced. A combination of both simulations and experimental calibrations enable high fidelity system group delay ($\frac{\partial \phi}{\partial \lambda}$) characterization in the whole visible spectral range. Finally, the signal processing techniques applied to the diagnostic signal are introduced and first measurements of 2D T_i maps are presented and validated against standard Charge eXchange Recombination Spectroscopy T_i profiles, finding excellent agreement.

Keywords: Wendelstein 7-X, ion temperature, Coherence Imaging Spectroscopy, Charge eXchange Recombination Spectroscopy

1. Introduction

All fusion experiments need to be equipped with diagnostics routinely providing reliable measurements of relevant parameters used to assess different properties of the plasma under investigation. In the Wendelstein 7-X (W7-X) stellarator [1, 2], Charge eXchange Recombination Spectroscopy (CXRS) [3, 4] is used to provide ion temperature (T_i) [5], impurity ion density (n_Z) [6] and impurity ion velocity flow (v_Z) [7] profiles. CXRS relies on the spectral analysis of radiation originating from ions present in the plasma that undergo Charge eXchange (CX) reactions mainly with neutrals injected by a neutral beam injection (NBI) system [8]. In a typical CXRS set-up light is collected by a fixed set of optical fibers displaced in the radial direction, allowing to obtain 1D profiles of the relevant parameters derived from measurements [5], assuming these as flux functions. The spatial resolution with

[4] See Sunn Pedersen *et al* 2022 (https://doi.org/10.1088/1741-4326/ac2cf5) for the W7-X Team.
[*] Author to whom any correspondence should be addressed.

which these profiles are obtained depends on the number of fibers used and their relative alignment with respect to the magnetic flux surfaces of the plasma.

In this work, a Coherence Imaging Charge Exchange Recombination Spectroscopy (CICERS) diagnostic is developed for W7-X. Using the Coherence Imaging Spectroscopy (CIS) technique [9] 2D T_i maps are obtained via the analysis of the 2D interference pattern generated by active CX radiation. The relevance of these maps reside in the ability to provide high spatial resolution T_i profiles, allowing for a more precise knowledge of their associated gradients and the opportunity to investigate possible asymmetries. The CIS technique is well established and has been routinely used for Scrape-Off Layer (SOL) flow velocity measurements in several fusion devices (e.g. MAST [10], DIII-D [11] or W7-X [12]). A first proof-of-principle demonstration of CIS for CX core plasma measurements was shown in the TEXTOR tokamak [13] where a scaling factor obtained from data derived from standard CXRS was used to derive absolutely calibrated 2D T_i maps. However, this technique has not been routinely applied to any plasma device. A system configuration optimization for the anticipated conditions at W7-X, as well as a simulation-based self-consistent approach for the calibration procedure of the diagnostic is introduced in this work. The calibration process, along with the background subtraction technique and further detailed signal treatment presented here enables the derivation of absolutely calibrated 2D T_i maps directly from the experimental CIS signal independently from additional experimental diagnostics for the first time.

The paper is structured as follows: the working principle of the diagnostic and the associated theoretical background is introduced in section 2. Section 3 covers the diagnostic synthetic model development, its design optimization and the experimental set-up. System characterization and calibration methods are introduced in section 4. Finally section 5 presents the results of the first measurements of the diagnostic, signal treatment and background subtraction. Experimental T_i maps are derived from the signal and validated against standard CXRS T_i profiles.

2. Theoretical background

The potential of the CIS technique resides in its ability to encode the spectral information of the collected light into a 2D interference pattern. In the spatial heterodyne configuration [9], a fringe pattern is generated by utilizing birefringent plates placed between two linear polarizers, which are oriented perpendicular (or parallel) to each other. The set of birefringent plates and polarizers is called the interferometric cell. The selection and arrangement of the plates ensure that the resulting interference pattern consists of parallel fringes along the frame. It is important to emphasize that the signal of the CIS diagnostic does not provide spectral resolution per se [9]. In order to ensure that the fringe pattern accurately encodes the desired features, a narrow bandpass filter (FWHM ~ 2 nm) centered on the emission line under study is introduced to the experimental setup. This filter prevents unwanted spectral features from being encoded in the fringe pattern. Other emission lines cannot be within the range of the narrow bandpass filter.

The purpose of CICERS is to measure the active CX radiation of low-Z impurity species. While several emission lines were considered, the main focus is put on the CVI($n' = 8 \rightarrow n = 7, \lambda_0 = 529.1$ nm) emission line, as carbon is the main impurity present in W7-X [5]. Results shown in this work focus on this particular emission line unless stated otherwise. In the core region of W7-X, ion temperatures of the order of $T_i \sim 2$ keV and strong magnetic fields ($B \sim 2.5$ T) are present. Under these conditions, it can be assumed that the main mechanisms contributing to the spectral lineshape of the CX emission line considered are the Doppler and multiplet (Zeeman + fine structure) effect.

The diagnostic fringe pattern S can be modelled as [9, 14]

$$S = \frac{I_0}{2}\left(1 + \zeta \cos\Phi\right) \tag{1}$$

where I_0 is the intensity of the measured radiation, ζ is the contrast of the fringe pattern and Φ is the phase shift introduced by the birefringent plates. Φ and ζ can be related to relevant ion parameters as follows:

(i) Φ is composed by [14]:

$$\Phi = \phi_0 + \underbrace{\arg\left(\sum_j I_j \mathrm{e}^{-i\lambda_0 \frac{\partial\phi}{\partial\lambda}\big|_{\lambda_0}\left(\frac{\lambda_j}{\lambda_0}-1\right)}\right)}_{\phi_\mathrm{M}} + \underbrace{\lambda_0 \frac{\partial\phi}{\partial\lambda}\bigg|_{\lambda_0} \frac{\boldsymbol{v}_Z \cdot \boldsymbol{l}}{c}}_{\phi_\mathrm{D}} \tag{2}$$

ϕ_0 is the intrinsic phase shift introduced for monochromatic radiation with $\lambda = \lambda_0$, where λ_0 is defined as the center-of-mass wavelength of the spectrum at rest. ϕ_M is the contribution due to the multiplet structure of the emission, where I_j is the normalized intensity of each of the multiplet component and λ_j its wavelength. The final term, ϕ_D accounts for the Doppler shift of the emission line, where $\boldsymbol{v}_Z \cdot \boldsymbol{l}$ refers to the ion velocity component parallel to the line-of-sight (LOS) of the diagnostic, c is the speed of light and $\frac{\partial\phi}{\partial\lambda}|_{\lambda_0}$ is the group delay, evaluated at λ_0.

(ii) ζ accounts for the different broadening mechanisms of the spectral lineshape. It can be described as [14, 15]:

$$\zeta = \zeta_\mathrm{I} \underbrace{\left|\sum_j I_j \mathrm{e}^{-i\lambda_0 \frac{\partial\phi}{\partial\lambda}\big|_{\lambda_0}\left(\frac{\lambda_j}{\lambda_0}-1\right)}\right|}_{\zeta_\mathrm{M}} \underbrace{\mathrm{e}^{-\frac{T_i}{2m_Z c^2}\left(\lambda_0 \frac{\partial\phi}{\partial\lambda}\big|_{\lambda_0}\right)^2}}_{\zeta_\mathrm{D}}. \tag{3}$$

The multiplet contrast, ζ_M, accounts for the fine structure of the spectral line and the Doppler contrast ζ_D accounts for the Doppler broadening, where T_i is the ion temperature and m_Z its mass. The instrument contrast ζ_I is an additional parameter added to account for the instrument response of the contrast, that can arise due to misalignments, crystal inhomogeneities and/or optical aberrations. Note that in this equation the impurity ion temperature (T_Z)

is assumed to be equal to the main ion temperature (T_i). The difference between these parameters can be assumed to be negligible for W7-X plasma scenarios [7].

The 2D maps of I_0, ζ and Φ can be recovered from the resulting interferogram via a 2DFFT-based demodulation routine. See [16, 17] for a detailed description of the procedure.

3. Diagnostic design

3.1. Synthetic model

The birefringent plate configuration of the system needs to be optimized for T_i and v_Z measurements for the foreseen plasma scenarios and expected conditions at W7-X. For this purpose, a synthetic model of the diagnostic has been developed. The phase shift ϕ introduced by the birefringent plates can be modelled with equation (12) in [18]. The ordinary and extraordinary refractive indices n_o and n_{ext} are computed via the Sellmeier equation [19]. The material considered for this work is α-BBO and the Sellmeier coefficients used are provided by the manufacturer. According to equations (2) and (3), not only the phase shift needs to be evaluated but also the group delay, $\frac{\partial\phi}{\partial\lambda}$, which is computed by taking the derivative of the phase shift with respect to λ, taking also into account the wavelength dependence of n_o and n_{ext} via the Sellmeier equation. Finally, the multiplet structure of each emission line considered is computed with a dedicated code available in the ADAS603 database [20–22], via an internal web interface [15]. The relevant information about the magnetic field used for these simulations is retrieved with the VMEC code [23, 24].

3.2. Crystal configuration optimization

The previously introduced model is used for the optimization of the set of plates that will be part of the diagnostic device. Several aspects need to be taken into account for the optimization of the crystal configuration:

(i) The spatial resolution of the diagnostic parallel to the fringes is determined by the pixel size, but in the direction perpendicular to the fringes is of the order of a fringe [15]. Because of this, a short fringe period is desired.
(ii) While high phase shift values should in principle enhance the velocity resolution, they might lead to low contrast values to the point where the fringe pattern cannot be observed because of the high T_i values expected in the plasma core of W7-X, resulting in a high level of phase shift noise propagated in the demodulation routine [14].

A Savart plate, consisting of two displacer plates with their respective birefringence planes displaced perpendicularly [9], is used to generate the parallel fringes. The thickness of each of these plates, L_{disp},is adjusted so as to provide the desired fringe period, and ideally no loss of contrast needs to be taken into account as the Savart plate produces zero phase shift for normal incidence. An additional delay plate is added to the system to provide an offset phase shift, approximately homogeneous throughout the screen. Since this component is the main contributor to the phase shift of the system, its thickness needs to be optimized for T_i and v_Z measurements. The total phase shift produced by the birefringent plates is modelled as:

$$\phi = \underbrace{\phi(L_{del}, \delta = \delta_{del}, \theta = 0^\circ)}_{\phi_{del}} + \underbrace{\phi(L_{disp}, \delta = \delta_{del}, \theta = 45^\circ) - \phi(L_{disp}, \delta = \delta_{del} + 90^\circ, \theta = 45^\circ)}_{\phi_{Sav}} \tag{4}$$

where L_{del} is the thickness of the delay plate, L_{disp} is the thickness of each of the individual displacer plates, δ_{del} defines the orientation of the delay plate birefringence plane and θ refers to the angle between the optical axis and the incidence surface contained in the birefringence plane of each plate. $\theta = 0^\circ$ for delay plates while $\theta = 45^\circ$ for displacer plates. Refer to [14, 16, 17] for a detailed description of the crystal angles defined here and further insight on the crystal simulations.

To investigate the effect of L_{del} on T_i resolution, a synthetic T_i profile peaked at 3 keV is imposed over the central horizontal array of pixels in the screen, with δ_{del} adjusted so as to obtain perpendicular fringes. The contrast variation for a 5% T_i variation, $\zeta(T_i) - \zeta(1.05T_i)$, along the synthetic profile is computed for several L_{del} values. Figure 1 shows that thicker plates provide better resolution for lower T_i while degrading it for higher T_i and viceversa. It can also be observed that the contrast gradient is not symmetric, since the group delay introduced by the Savart plate varies in the direction perpendicular to the fringes, see figure 5.

For the v_Z resolution consideration, the expected Doppler contribution to the phase shift ϕ_D for a flow of $v_Z = 1\,\mathrm{km\,s^{-1}}$, provided by the last term in equation (2), is compared to the estimated phase shift noise propagated in the demodulation process σ_Φ as a function of L_{del} for constant temperatures of $T_i = 3$ keV and $T_i = 1.5$ keV in the central pixel of the image. σ_Φ is estimated by generating a set of fringe patterns varying its contrast from 0.1 to 1 adding gaussian noise assuming a camera signal-to-noise (SNR) ratio of 40 dB, while the dynamic range of the camera used in this work is ∼80 dB (see section 3.3). While this estimation is not a best-case scenario,

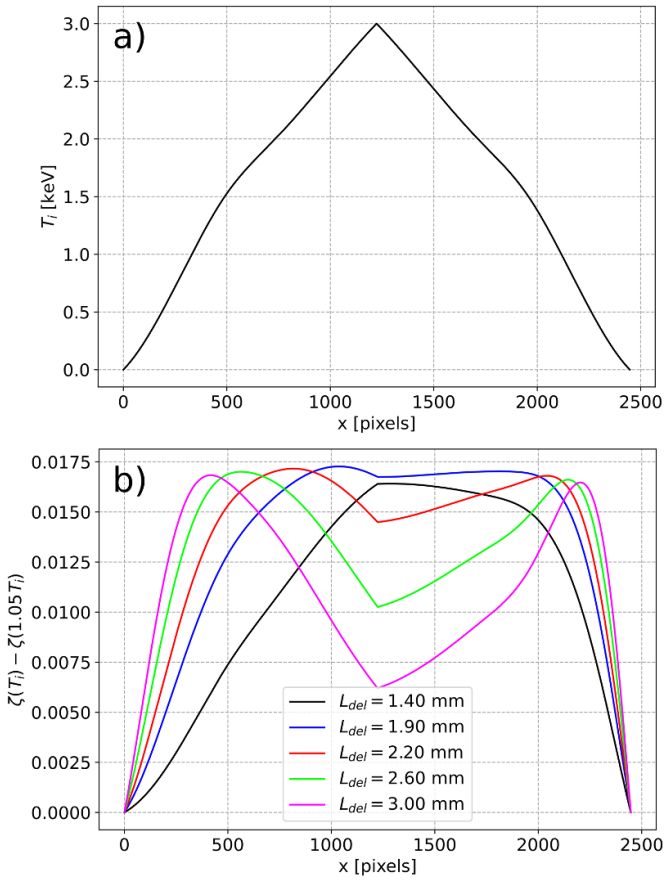

Figure 1. (a) Synthetic T_i profile and (b) L_{del} scan for the contrast change for a 5% T_i change along the profile considering the CVI emission line.

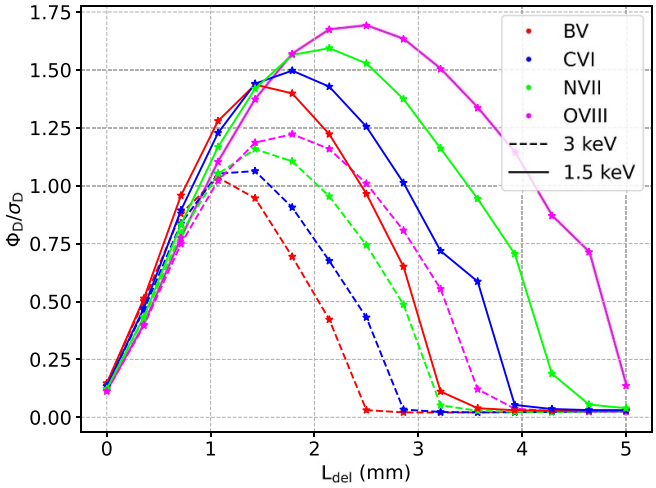

Figure 2. Signal to Noise phase shift ratio estimation for a flow of $v_Z = 1\,\mathrm{km\,s^{-1}}$. The Doppler phase shift contribution is compared to phase shift noise propagated in the demodulation process due to contrast loss. Ratio scan for L_{del} values. Several impurity ion emission lines are considered.

it is optimistic attending to the noise levels observed in the experimental measurements shown in section 5.

In this case, several emission lines are considered. Results are shown in figure 2. The ion impurity flow velocity resolution is constrained by the loss of contrast due to high temperatures in the plasma core, shown by the different maximum SNR of the solid and dashed curves. While this effect can be alleviated by the use of filter boxes in demodulation routine, see section 5, similar phase shift levels (and thus velocity resolution) as the SOL CIS diagnostic at W7-X [12] cannot be achieved.

In view of these simulations, an α-BBO delay plate with thickness $L_{\mathrm{del}} = 2.5$ mm is chosen. The choice of L_{del} is made in order to prioritize the resolution in T_i measurements while retaining as much v_Z resolution as possible. The achievable resolution ($\sim$1 km s^{-1}) is expected to be sufficient to resolve the estimated velocity measurements. An additional Savart plate, composed by two α-BBO displacer plates with thicknesses $L_{\mathrm{disp}} = 10$ mm, is added to generate the desired fringe pattern. Such values of L_{disp} are determined to provide a fringe period of $\sim$8 pixels per fringe.

3.3. Experimental set up

CICERS was installed towards the end of the OP2.1 experimental campaign at W7-X, in February 2023. It shares the same plasma view as the toroidal SOL CIS system. For a detailed description of the SOL CIS and plasma light collection system, see [5, 12]. Figure 3 shows the different component of both systems. CICERS utilizes the same camera model as SOL CIS [12] (element 1: pco.edge 5.5 CLHS), as well as the same set of lenses (element 2 and 7a: Zeiss $f = 135$ mm, $f/2$; element 7b and 8: Nikon $f = 50$ mm, $f/1.4$). Both the plasma light (coming from element 8) and calibration light (coming from element 10) go through a 50:50 beamsplitter (element 9).

Light is then collimated by the lens tandem (element 7a+7b) and redirected with a mirror (element 6). A set of 4 narrow bandpass filters (FWHM= 2 nm) is placed in a high speed filter wheel (element 5). Each filter is centered around one of the 4 emission lines chosen to enable measurements of different low-Z impurity species, namely: HeII($n' = 4 \rightarrow n = 3, \lambda_0 = 468.6$ nm), CVI($n' = 8 \rightarrow n = 7, \lambda_0 = 529.1$ nm), NVII($n' = 9 \rightarrow n = 8, \lambda = 566.9$ nm) and OVIII($n' = 10 \rightarrow n = 9, \lambda = 606.8$ nm).

The complete system is installed in the AEA21 port, see figure 4. Its view is oriented towards NBI sources S3 and S4, located in half module 20 of the vacuum vessel. A spatial calibration of the camera view with experimental frames of passive radiation has been carried out using the Calcam software [25]. Figure 4 shows (a) the vessel view obtained from the CAD model after the spatial calibration is performed overlaid with an example of an experimental frame of passive radiation obtained with the HeII filter, which provides better insight on the W7-X vessel structures used for the spatial calibration than the CVI filter, and (b) the obtained plasma view with NBI S4 and S3 with the main plasma. As the majority of the W7-X plasma facing components are made of carbon, no artifacts due to reflections are expected nor observed in the experimental data [26], see figure 4(a) as reference.

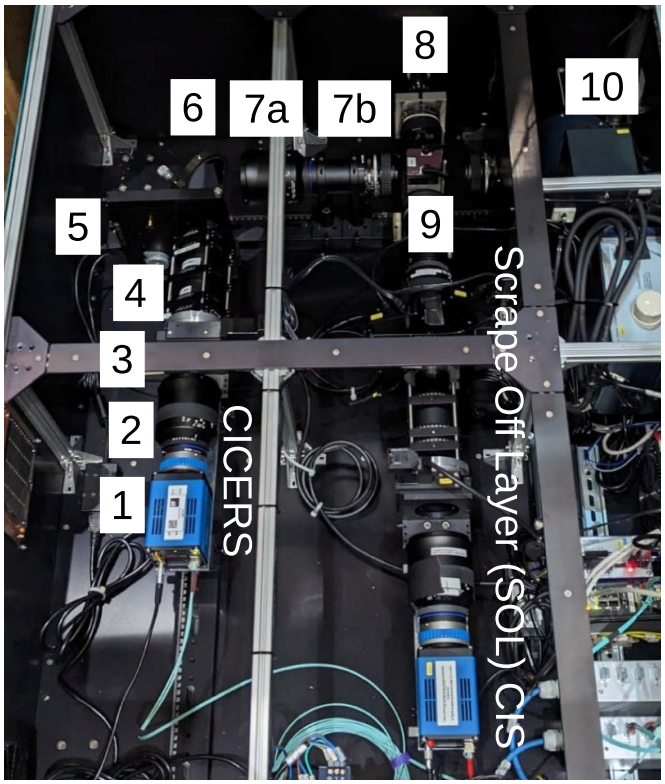

Figure 3. Experimental setup of both CICERS and Scrape Off Layer (SOL) CIS diagnostics at W7-X during OP2.1.

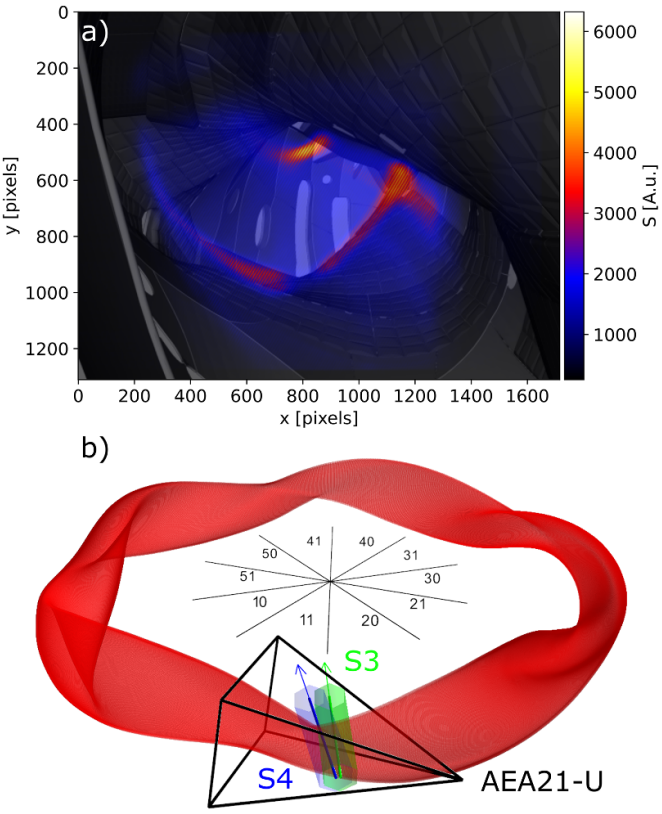

Figure 4. (a) Vessel CAD view of the diagnostic obtained by the spatial calibration overlaid with an experimental frame of passive HeII radiation and (b) diagnostic view with the main plasma volume in red and NBI S3 and S4 nominal injection directions.

According to the method used for the spatial localization of the active CX radiation, an averaged pixel-to-pixel spatial resolution of 1 mm is achieved for the complete field of view of the diagnostic. Please refer to section 5.1 for further insight on spatial localization. Nonetheless, the true spatial resolution is set by one of the collimating lenses (element 7a), which is defocused to the point where the individual fibers of the fiber bundle (used to direct the collected radiation to the diagnostic) are barely seen. Since a single fiber takes 8 pixels in the camera, the true spatial resolution of the system is about 8 mm, which is the same as expected in the direction perpendicular to the fringes for the interferogram fringe period obtained.

4. System characterization and calibration process

The main quantities to be determined for T_i measurements are the group delay $\frac{\partial\phi}{\partial\lambda}$ and the instrument contrast ζ_{I}. CICERS uses the C-WAVE laser, a widely tunable, continuous-wave laser for calibration purposes, as done by the SOL CIS [12, 27]. The laser emits monochromatic light, which, combined with an Ulbricht sphere, generates raw CICERS interferograms. These images can be demodulated to determine ϕ_0 and ζ_{I} at given λ_0. The main emission line routinely measured by CICERS is CVI ($\lambda = 529.1$ nm), whose wavelength lies outside the range of the C-WAVE laser (450–525 nm; 532 nm; 540–650 nm). Because of this, neither ϕ_0 nor $\frac{\partial\phi}{\partial\lambda}|_{\lambda_0}$ calibrations can be performed directly for the CVI emission line. However, given that this line is the best candidate for CICERS purposes attending to the requirements previously introduced, an indirect approach for the determination of $\frac{\partial\phi}{\partial\lambda}|_{\lambda_{\mathrm{CVI}}}$ has been developed based on the simulation of the group delay. Since the simulation depends on parameters which are not sufficiently accurately known, a correction is determined from calibration scans at several other wavelengths that are accessible to the C-WAVE laser.

$\frac{\partial\phi}{\partial\lambda}|_{\lambda_0}$ can be experimentally determined with the C-WAVE laser by performing a laser scan with steps of $\Delta\lambda \sim 5$ pm around a given λ_0. In this range, $\frac{\partial\phi}{\partial\lambda}$ is assumed to behave linearly and can be determined with a linear fit of the data [27]. Routine calibrations of the group delay are not performed since group delay drifts due to laboratory temperature changes are assumed to be negligible. In order to solve the lack of direct measurements at the observed wavelength, several laser scans in the C-WAVE accessible range have been performed to improve the group delay simulations. An example of a reference laser scan and the resulting group delay in the whole image for $\lambda \sim 464.875$ nm is shown in figure 5.

Experimental $\frac{\partial\phi}{\partial\lambda}|_{\lambda_0}$ are compared with simulation results, using the nominal manufacturing parameters of the components. Note that the the discrepancies between simulations with

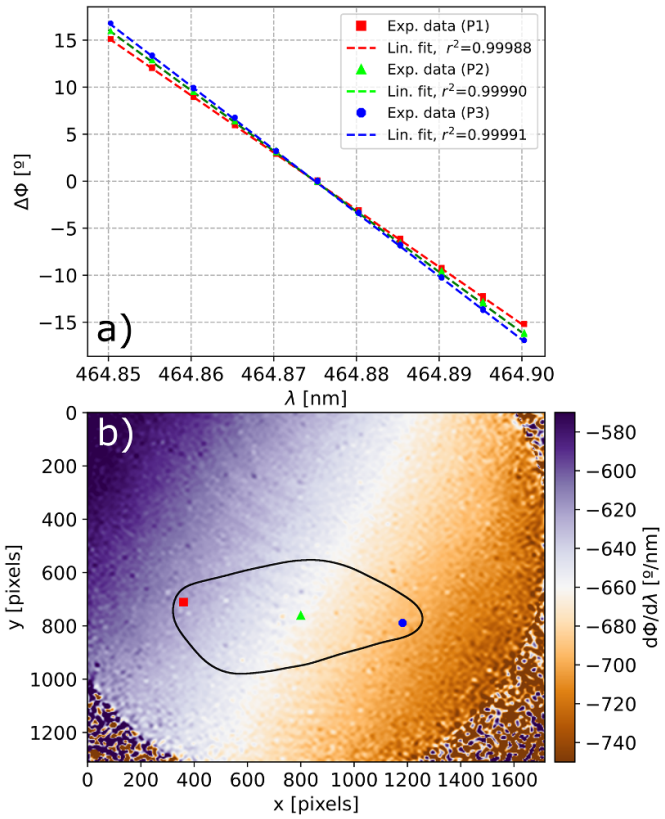

Figure 5. (a) Phase shift increment ($\Delta\phi = \phi(\lambda) - \phi(\lambda_0)$) against wavelength for the laser scan around $\lambda_0 \sim 464.875$ nm and linear fit of the data for pixels P1, P2 and P3 shown in (b) and (b) Group delay result in the whole image for the laser scan. The typical experimental NBI ROI is enclosed within the black line.

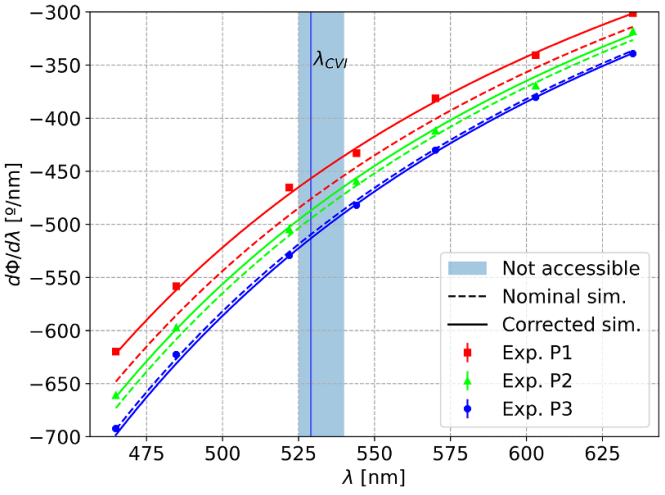

Figure 6. Group delay experimental and simulated (both nominal and corrected) values in the visible range for pixels shown in figure 5.

nominal parameters and experimental values are due to inaccuracies in the parameters used and crystal inhomogeneities.

Figure 6 plots the resulting values for the laser scans performed in the pixels indicated in figure 5, where a clear difference between simulated and experimental values can be

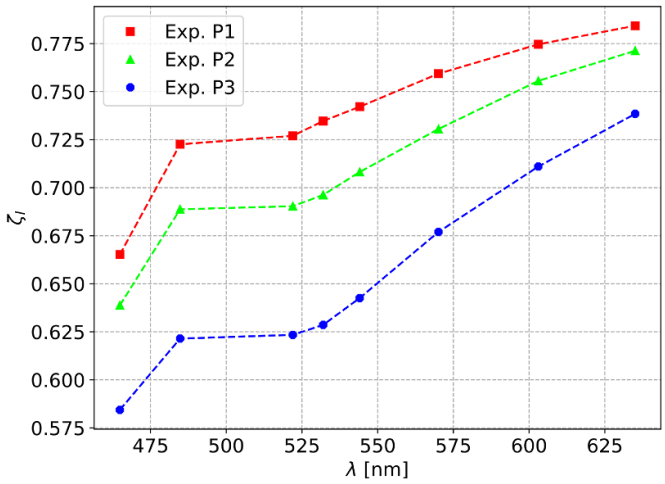

Figure 7. Instrument contrast ζ_I scan in the visible range for pixels P1, P2 and P3 shown in figure 5.

observed. A correction factor defined as the mean of the relative error between the experimental data and nominal simulations is computed. Applying the correction factor to the nominal simulations, the experimental group delay can be reproduced with high precision by simulations in the visible range, as shown by the solid lines in figure 6. Reevaluating the relative error between the simulated corrected $\frac{\partial\phi}{\partial\lambda}|_{\lambda_0}$ and experimental values, a mean relative error $\Delta\partial_\lambda\phi = 0.5\%$ is found, which is considered as the systematic error of the simulations raised because of the assumption that the relative error is constant in the whole visible range. In view of this result, these simulations are used to compute $\frac{\partial\phi}{\partial\lambda}|_{\lambda_{\rm CVI}}$, that lies within the region not accessible by the C-WAVE laser.

The instrument contrast ζ_I can be inferred from a single fringe pattern generated at the desired λ_0. Changes due to laboratory temperature drifts are also assumed to be negligible because of the nature of this parameter (experimental misalignment of the components, crystal inhomogeneities and optical aberrations). The instrument contrast values from the fringe patterns generated in the previous laser scans in the pixels shown in figure 5 are plotted in figure 7. An additional value at ~532 nm is added, obtained by the generation of a fringe pattern with an Nd:YAG laser, which is used by the C-WAVE laser for tuning purposes. While a clear dependence of ζ_I with respect to λ_0 is observed within the visible range, it is nonetheless small for the interpolation range of interest for our application, and $\zeta_I(\lambda_{\rm CVI})$ is determined with a linear interpolation of the available data.

5. First measurements

Raw experimental frames have a non-negligible contribution of background radiation, namely passive CVI and bremsstrahlung, not blocked by the narrow bandpass filter. As both their intensities are of the same order of magnitude as the active CX radiation, methods to isolate the active CX radiation from the other contaminants are needed. The total CICERS signal can be expressed as [13]

$$S = \underbrace{I_{\mathrm{CX}}\left(1+\zeta_{\mathrm{CX}}\cos\Phi_{\mathrm{CX}}\right)}_{S_{\mathrm{CX}}} + \underbrace{I_{\mathrm{Bkg}}\left(1+\zeta_{\mathrm{Bkg}}\cos\Phi_{\mathrm{Bkg}}\right)}_{S_{\mathrm{Bkg}}} \quad (5)$$

where the subscripts CX and Bkg refers to the active CX and background contributions to the signal S respectively. The approach followed here to isolate S_{CX} consists on the estimation and subtraction of S_{Bkg} from S.

When NBI modulation is performed, S_{Bkg} can be estimated as the linear interpolation between raw frames taken right before and after each NBI blip, as done by the main CXRS system [5]. While this method has shown to provide good results with CICERS, the linear interpolation of the passive radiation is only valid for NBI injection up to ∼60 ms [5]. After this time, the temporal evolution of the passive CX intensity is shown to change in its linear tendency. Moreover, the non-linear increase of n_e during NBI injection implies an increase of the Bremsstrahlung radiation emissivity as $\varepsilon_B \propto n_e^2$ [28]. In order to estimate the contribution of these effects, and taking advantage of the 2D view provided by CICERS, an ROI-scaled background subtraction procedure is used. The different steps applied for this are the following:

(i) Perform a linear interpolation of the background signal from frames taken right before and after NBI injection.
(ii) Compute the mean of the ratio of intensity in the raw experimental frame to intensity in the linearly interpolated background frame in a predefined ROI. The ROI is chosen so that the pixels within it are spatially located outside the plasma separatrix (see section 5.1). Assumming the CVI impurity density outside the separatrix to be negligible, the sources of radiation present in this ROI are all passive CVI and bremsstrahlung.
(iii) Multiply the background interpolated frame by the computed ratio and substract it from the raw experimental frame.

An example of the application of this method is shown in figure 8. Figure 8(a) shows the normalized trace of the total raw signal (active CX+background) in black, defined as the sum of the intensity of the signal in the whole image, the trace of the background signal obtained by the ROI-scaled method is plotted in blue and the signal of the current of the NBI sources S4 and S7 are plotted in red and green respectively. Frames chosen for interpolation are the first frames right before and after NBI S4 injection. In this particular discharge, several NBI S7 blips lasting $\tau_{\mathrm{blip}} = 125$ ms were performed. The radiation increase and decrease due to the S7 blips can be observed in the total signal trace but is roughly temporally resolved since the exposure time used for this discharge is $\tau_{\mathrm{exp}} = 50$ ms. As shown by the interpolated background trace, the ROI-scaled method is able to mimick this behaviour, which otherwise would not be reproduced with a simple linear interpolation of the data. Figure 8(b) shows an example of a single raw 2D interferogram frame, where the ROI is within the green line and the contour of the typical active CX region is plotted in red for comparison. This method has proven to provide

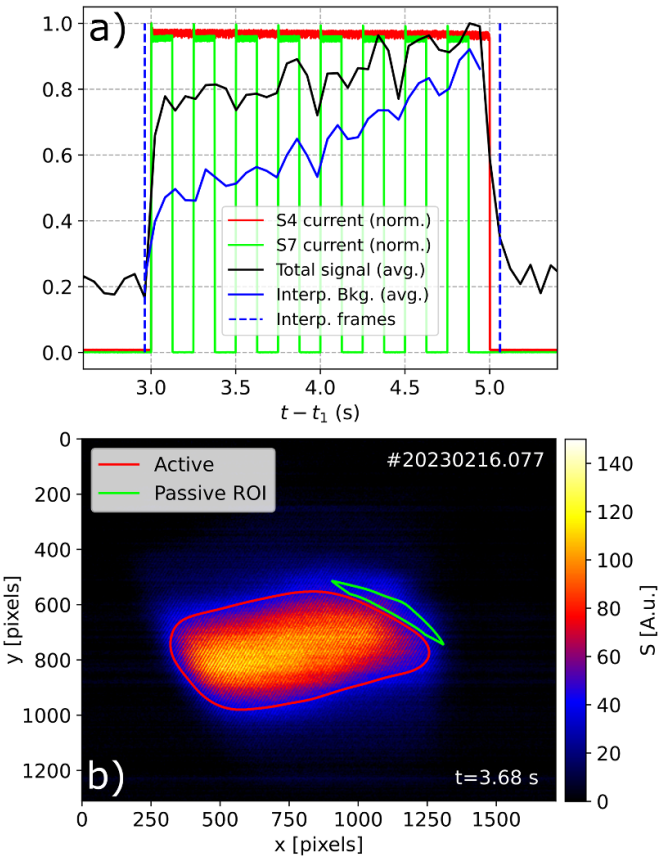

Figure 8. (a) Experimental trace of the total CICERS signal (black) and the interpolated background signal (blue) and normalized NBI S4 and S7 currents (red and green, respectively) for discharge #20230216.77 and (b) example of the total raw signal obtained in an experimental frame, with typical active CX region shown in red and ROI, in green, used for the ROI-scaled background subtraction.

good results in low density plasmas up to $\int n_e \mathrm{d}l \sim 5 \cdot 10^{19}\ \mathrm{m}^{-2}$ with NBI injection in ECRH plasmas both with NBI blips and continuous injection up to 2 s, see section 5.1. However it just provides a non-rigourous rough estimate of S_{Bkg}. It is only valid for scenarios where either the background contribution does not significantly evolve between interpolation frames (i.e. NBI S4 blips) or the background signal is small compared to the active CX contribution (low n_e). The development of a rigorous approach to deal with the S_{Bkg} component of the signal considering its different contributions (passive and Bremsstrahlung) is foreseen, and will be subject of future work.

In general, short exposure times of the order of $\tau_{\mathrm{exp}} \sim 20$–50 ms were used. Due to the low transmission of the optical layout and the low intensity of the CX radiation, experimental frames are considerably affected by noise, see figure 8(b) as an example.

Noise levels are critical in the assesment of the interferogram parameters, as it can lead to considerable error propagation in the demodulation process. This effect can be mitigated in the 2D FFT demodulation routine. In Fourier space,

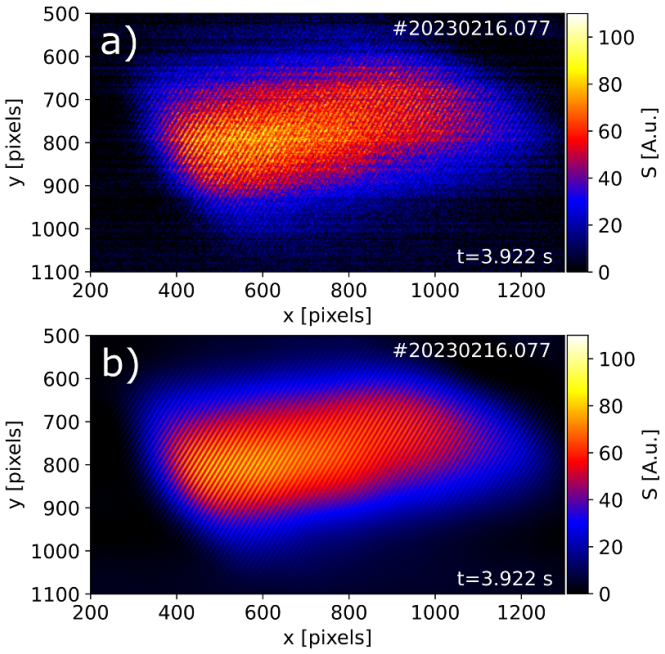

Figure 9. (a) Raw experimental active frame after background subtraction and (b) same frame after denoising.

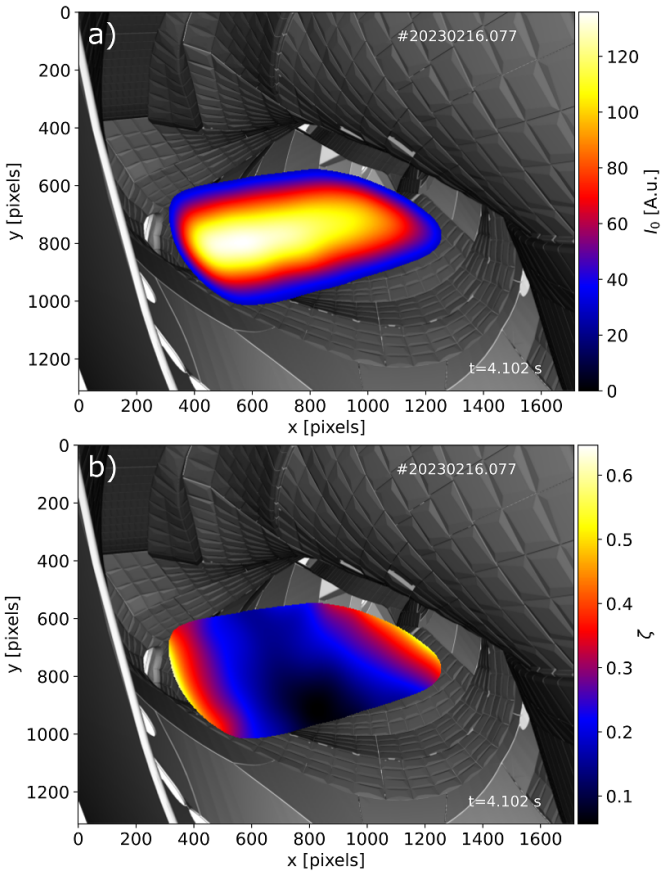

Figure 10. Main parameters of an experimental frame recovered after demodulation. (a) is the intensity I_0, (b) is the contrast ζ.

the experimental signal of the interferogram manifests as a set of three peaks $(I(0), I(\pm))$ [16, 17]. As demonstrated analytically in appendix B.1.1 in [29], the effect of Fourier-domain filtering is to reduce the noise variance, assuming normally distributed uncorrelated noise in each pixel. In view of this result, the effect of noise can be reduced by using narrow filter boxes adjusted to the $I(0)$, $I(\pm)$ peaks. Figure 9 shows the effect of Fourier-domain filtering to a frame of active CX signal.

Finally, the intensity I_0, and contrast ζ are recovered with the already mentioned demodulation routine and shown in figure 10.

5.1. 2D T_i maps

The ion temperature T_i is linked with ζ as shown in equation (3). T_i can be evaluated as [15]:

$$T_{\mathrm{i}} = -\frac{2m_Z c^2}{\left(\lambda_0 \left.\frac{\partial\phi}{\partial\lambda}\right|_{\lambda_0}\right)^2}\left[\log\left(\frac{\zeta}{\zeta_{\mathrm{I}}}\right) - \log\left(\zeta_{\mathrm{M}}\right)\right]. \qquad (6)$$

The multiplet structure of the emission, computed as explained in section 3.1, is needed for ζ_{M}, for which local values of the magnetic field are also necessary. As done in standard CXRS, the active CX radiation is assumed to be localized in the point of closest approach between the line of sight assigned to each pixel in the spatial calibration and the nominal beam axis for the complete diagnostic field of view. Thus, each pixel in the CICERS field of view has an independent spatial location assigned. This localization method has been found to be consistent with simulation results for toroidally oriented LOS [6] for CXRS. Once localized, the magnetic field $\boldsymbol{B}$ and effective radius r_{eff} are computed with VMEC [23, 24] for each individual pixel.

Previous analysis carried out for the standard CXRS estimated the FWHM of the active CX emissivity distribution along the LOS to range from $\sim$1 cm in the core up to $\sim$4 cm towards the edge in terms of r_{eff} for its toroidal view [5], as a consecuence of having these LOS almost parallel to the flux surfaces across the beam width. Being in an equivalent view, CICERS data is expected to behave similarly, rendering similar well-localized measurements. Nonetheless, this aspect will be confirmed and further investigated for CICERS in future work.

Both the group delay error $(\Delta\partial_\lambda\phi)$ and the statistical error of the contrast $(\Delta\zeta)$ propagated in the demodulation routine have been taken into account to compute the error propagation in T_{i} according to equation (6). A homogeneous group delay error of $\Delta\partial_\lambda\phi = 0.5$ % is used, according to the results found in section 4. The statistical error of the contrast $\Delta\zeta$ is assessed via a look-up table. A series of synthetic interferograms replicating the experimental interferogram is generated, scanning over different values of intensity $(10 < I_0 < 200$ counts) and contrast $(0.1 < \zeta < 0.8)$. Typical experimental I_0 and ζ lie within these values. A source of gaussian noise with standard deviation $\sigma_N = 7.5$ camera counts is added to the interferogram. The noise standard deviation σ_N is determined by performing a gaussian fit of the noise distribution obtained from

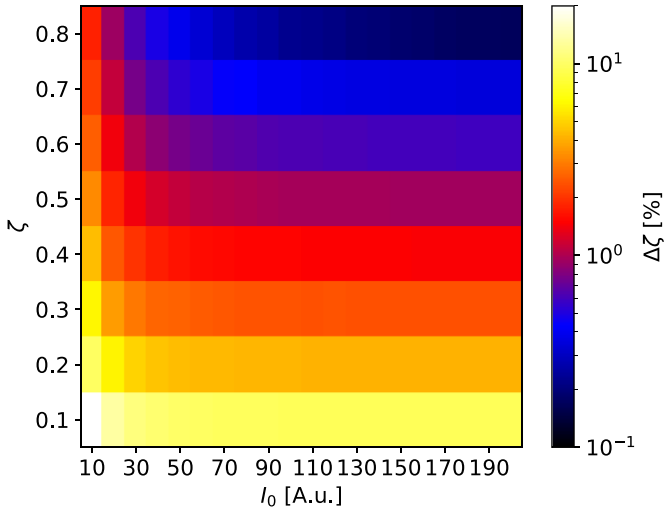

Figure 11. Contrast statistical relative error ($\Delta\zeta$) look-up table used for T_i error propagation. Note the logarithmic scale used on the colorbar.

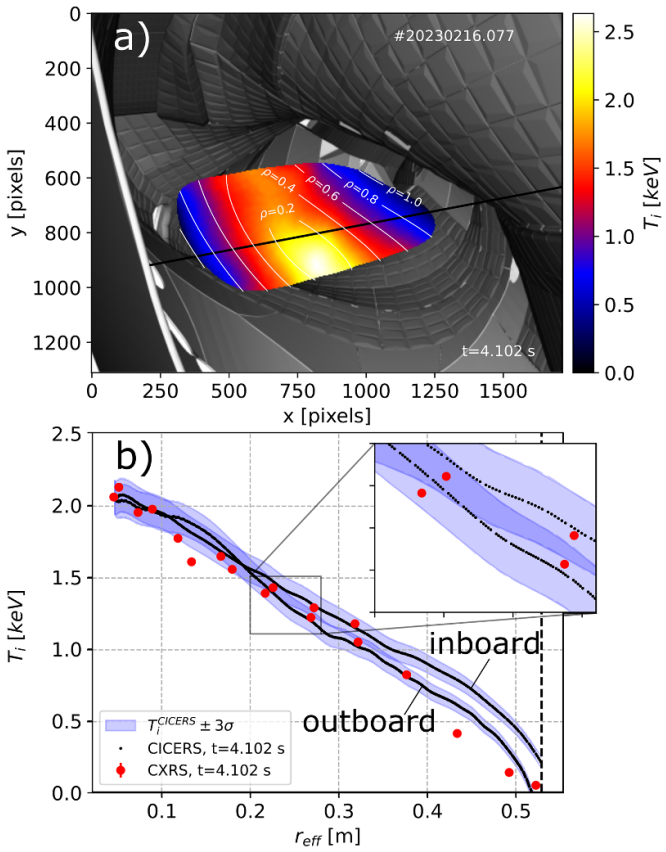

Figure 12. (a) 2D T_i map and NBI S4 nominal injection direction overlaid with contours of magnetic flux surfaces computed with VMEC and (b) T_i profile in the NBI S4 injection direction with estimated $\pm 3\sigma$ confidence interval, and comparison against T_i values from the toroidally oriented view of CXRS for discharge #20230216.77 ($\int n_e dl \sim 2$–$3 \cdot 10^{19}$ m^{-2}, $\tau_{exp} = 50$ ms) using the ROI-scaled background subtraction method.

experimental dark frames. From the synthetic interferograms, $\Delta\zeta$ is determined by the comparison of the demodulated ζ against the synthetic one. Each iteration is repeated 100 times. The resulting look-up table of the statistical relative error of the contrast is shown in figure 11. Note the logarithm scale used and the small dependence of the error with I_0 as a consequence of the image denoising introduced in the previous section. An individual $\Delta\zeta$ is assigned to each pixel according to its ζ and I_0.

Figure 12(a) shows an experimental 2D T_i map for discharge #20230216.77 (line-integrated density of $\int n_e dl \sim 2$–$3 \cdot 10^{19}$ m^{-2}, $\tau_{exp} = 50$ ms) overlaid with contours of magnetic flux surfaces computed with VMEC. The ROI-scaled background subtraction method previously introduced has been applied in the analysis of the data. Figure 12(b) shows a profile obtained from the 2D data showed in (a) in the nominal NBI S4 injection direction, indicated as the black line in figure 12(a). The blue area corresponds to the $\pm 3\sigma$ confidence interval of the measurements. The two CICERS lines shown in the plot correspond to measurements in the inboard and outboard side of the plasma and the perceived asymmetry is thought to be due to inaccuracies in the magnetic equilibrium. The CXRS toroidal view T_i data is plotted for comparison. Note the enhanced spatial resolution of CICERS compared to CXRS in the zoom of figure 12(b), where each point corresponds to the measurement in each single pixel.

In this particular discharge, continuous injection was carried out by NBI S4 (seen by CICERS) while NBI blips of 125 ms were performed by NBI S7 (seen by CXRS). Several T_i profiles along the NBI S4 injection direction during the injection time are obtained and compared to CXRS data, see figure 13. In general, excellent agreement is found between CICERS and CXRS data when comparing the profiles derived from 2D images in the equivalent CICERS view, which corresponds to the nominal NBI S4 injection direction indicated with the solid black line in figure 12(a). While the core T_i inferred from the extrapolation based on the data obtained in the NBI injection direction (observed both by CICERS in NBI S4 and CXRS in NBI S7) is $T_i^{core} \sim 2.1$–2.2 keV, a maximum core $T_i \sim 2.5$ keV is observed within the CICERS field of view. This fact illustrates the importance of true core measurements as opposed to profile extrapolation. In this case, the inference of core values from profile extrapolation does not provide reliable results due to inaccuracies in the magnetic equilibrium used and flux surface mapping. A systematic discrepancy can also be found towards the edge, where CICERS predicts higher T_i values than CXRS. A possible reason for this discrepancy may be an overestimation of the background radiation in this region, where the active CX intensity is lower, due to the background subtraction approach. Nonetheless, CXRS T_i profiles also suffer from background subtraction issues, tending to underestimate T_i in this region.

An additional 2D T_i map corresponding to discharge #20230316.28 (line-integrated density of $\int n_e dl \sim 4$–$5 \cdot 10^{19}$ m^{-2}, $\tau_{exp} = 20$ ms) is shown in figure 14(a). In this figure, the resulting T_i map obtained with blips in NBI S4 and continuous injection in NBI S7 using the ROI-scaled background subtraction method introduced previously is shown.

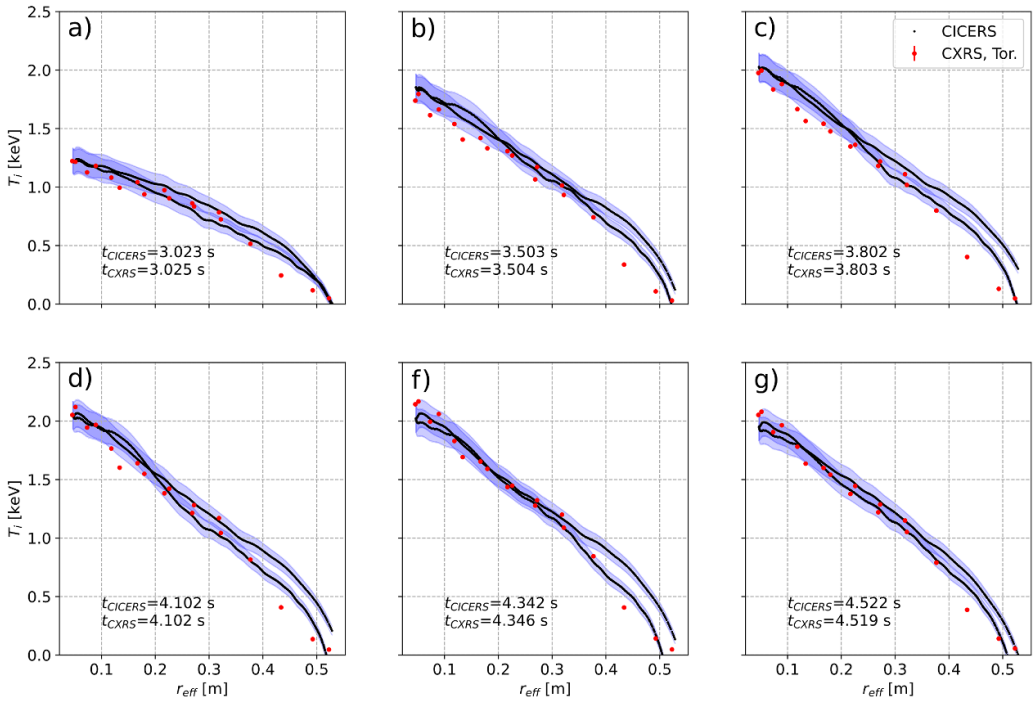

Figure 13. Comparison of the T_i profile evolution throughout NBI S4 continuous injection in discharge #20 230 216.77. CICERS data is taken along NBI S4 nominal injection direction shown in figure 12. The ROI-scaled background subtraction method is used in the analysis.

Also, results on the profiles obtained from the solid black line indicated in (a) using both ROI-scaled and simple linear background subtraction methods are plotted for comparison in figure 14(b). It can be observed that the ROI-scaled background subtraction (green profile) prevents the inboard-outboard T_i discrepancies observed with the linear interpolation background subtraction (blue profile). Moreover, better agreement to CXRS data is found for the ROI-scaled profile, while also showing the higher T_i prediction on the core and the discrepancy towards the edge as previously commented.

6. Conclusions and future work

A new CICERS diagnostic has been set up and installed at W7-X. The working principle and basics of the diagnostic have been introduced and applied to develop a synthetic model of the diagnostic. The synthetic diagnostic is used both for the optimization of the components and a method for the calibration of $\frac{\partial\phi}{\partial\lambda}$ based on the comparison of simulations with experimental calibration data using the C-WAVE tunable laser. This method is able to reproduce the group delay in the visible range ($\lambda \sim$450–630 nm) with high precision, $\Delta\partial_\lambda\phi \sim 0.5\%$. First measurements with the diagnostic have been carried out and a first approach to estimate and substract the background contribution of the signal is introduced. It has proven to be useful for scenarios where the background contribution does not significantly evolve between interpolation frames (i.e. NBI S4 blips) or the background signal is small compared to the active CX contribution (low n_e). The development of a rigorous approach to deal with the background contribution of the signal will be addressed in future work. A method to deal with high noise levels is also shown. T_i maps are derived from the experimental signal independently from additional diagnostics for the first time and compared to CXRS T_i profiles. Excellent agreement is found between CXRS and CICERS derived T_i profiles, reaffirming the validity of the signal processing methodology and calibration methods used in this work for the experimental scenarios explored. The maximum T_i found within the CICERS field of view is 2.5 keV, corresponding to the true plasma core T_i. On the other hand, the core T_i inferred from extrapolation of the standard CXRS profile is $T_i \sim$2.1–2.2 keV. CICERS measurements constitute an enhancement on spatial resolution with respect to CXRS and is also capable of performing true core T_i measurements, which are shown to be higher than the extrapolated estimates from the CXRS profiles due to inaccuracies in the magnetic equilibrium and flux surface mapping.

Several improvements of the diagnostic are foreseen for the next experimental campaign. A rearrangement of the components so as to optimize the system transmission and light output will be performed, as well as finer alignment of the components and more precise calibrations. Finally, the derivation of n_Z and v_Z maps will be addressed, exploiting the full potential of the diagnostic.

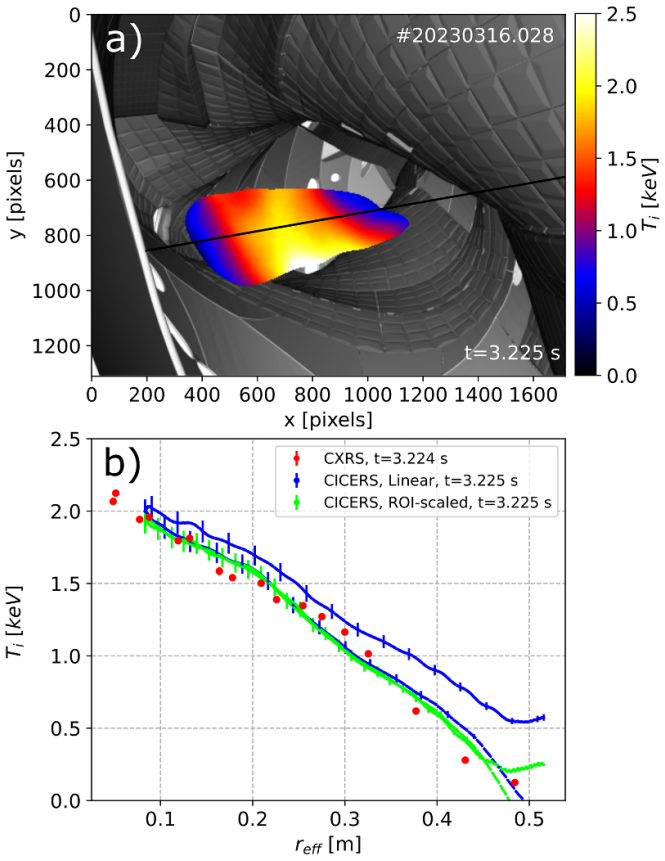

Figure 14. (a) 2D T_i map obtained with NBI blips using the ROI-scaled background subtraction and (b) Comparison of T_i profiles in the direction shown in (a) obtained with linear interpolation (blue) and ROI-scaled (green) background subtraction. Toroidally oriented CXRS T_i profile is also shown for comparison. Data corresponds to discharge #20230316.28 ($\int n_e dl \sim 4$–$5 \cdot 10^{19}$ m^{-2}, $\tau_{exp} = 20$ ms).

Data availability statement

The data cannot be made publicly available upon publication due to legal restrictions preventing unrestricted public distribution. The data that support the findings of this study are available upon reasonable request from the authors.

Acknowledgment

R L C and E V gratefully acknowledge the financial support of the European Research Council (ERC) under the European's Union Horizon 2020 research innovation program (Grant Agreement No. 805162) and the Ministerio de Ciencia e Innovación under the PID program (Grant Agreement No. PID2020-116822RB-I00). This work has partially been carried out within the framework of the EUROfusion Consortium, funded by the European Union via the Euratom Research and Training Programme (Grant Agreement No. 101052200–EUROfusion). Views and opinions expressed are however those of the author(s) only and do not necessarily reflect those of the European Union or the European Commission. Neither the European Union nor the European Commission can be held responsible for them.

ORCID iDs

R Lopez-Cansino https://orcid.org/0009-0003-5806-2992
V Perseo https://orcid.org/0000-0001-8473-9002
E Viezzer https://orcid.org/0000-0001-6419-6848
D M Kriete https://orcid.org/0000-0002-3657-2911
O P Ford https://orcid.org/0000-0002-5646-4758
T Romba https://orcid.org/0000-0002-2727-9385
P Zs Poloskei https://orcid.org/0000-0001-7781-5599

References

[1] Wolf R *et al* 2017 *Nucl. Fusion* **57** 102020
[2] Wolf R *et al* 2019 *Phys. Plasmas* **26** 082504
[3] Fonck R, Darrow D and Jaehnig K 1984 *Phys. Rev.* A **29** 3288
[4] Fonck R J 1985 *Rev. Sci. Instrum.* **56** 885–90
[5] Ford O *et al* 2020 *Rev. Sci. Instrum.* **91** 023507
[6] Romba T *et al* 2023 *Plasma Phys. Control. Fusion* **65** 075011
[7] Alonso J *et al* 2022 *Nucl. Fusion* **62** 106005
[8] Spanier A *et al* 2021 *Fusion Eng. Des.* **163** 112115
[9] Howard J 2010 *J. Phys. B: At. Mol. Opt. Phys.* **43** 144010
[10] Silburn S, Harrison J R, Howard J, Gibson K, Meyer H, Michael C and Sharples R 2014 *Rev. Sci. Instrum.* **85** 11D703
[11] Howard J *et al* 2011 *Contrib. Plasma Phys.* **51** 194–200
[12] Perseo V, Gradic D, König R, Ford O P, Killer C, Grulke O and Ennis D A 2020 *Rev. Sci. Instrum.* **91** 013501
[13] Howard J, Jaspers R, Lischtschenko O, Delabie E and Chung J 2010 *Plasma Phys. Control. Fusion* **52** 125002
[14] Silburn S 2014 A Doppler Coherence Imaging Diagnostic for the Mega-Amp Spherical Tokamak atlA Doppler coherence imaging diagnostic for the mega-amp spherical tokamak *PhD Thesis* Durham University
[15] Gradic D *et al* 2021 *Nucl. Fusion* **61** 106041
[16] Gradic D 2018 Doppler coherence imaging of ion dynamics in the plasma experiments VINETA. II and ASDEX Upgrade *PhD Thesis* Technischen Universität Berlin
[17] Perseo V 2020 Impurity flow measurements with Coherence Imaging Spectroscopy at Wendelstein 7-X Universität Greifswald Universität Greifswald
[18] Veiras F E, Perez L I and Garea M T 2010 *Appl. Opt.* **49** 2769–77
[19] Sellmeier W 1872 *Ann. Phys., Lpz.* **223** 386–403
[20] Hey J, Chu C, Brezinsek S, Mertens P and Unterberg B 2002 *J. Phys. B: At. Mol. Phys.* **35** 1525
[21] Hey J, Chu C, Mertens P, Brezinsek S and Unterberg B 2004 *J. Phys. B: At. Mol. Phys.* **37** 2543
[22] Summers H 2004 *The ADAS User Manual* (available at: www.adas.ac.uk/)
[23] Hirshman S P and Whitson J 1983 *Phys. Fluids* **26** 3553–68
[24] Grahl M, Svensson J, Werner A, Andreeva T, Bozhenkov S, Drevlak M, Geiger J, Krychowiak M and Turkin Y 2018 *IEEE Trans. Plasma Sci.* **46** 1114–9
[25] Silburn S *et al* 2022 Calcam (https://doi.org/10.5281/zenodo.10655746)
[26] Carr M *et al* (ASDEX Upgrade Team, JET Contributors, MAST-Upgrade Team, EUROfusion MST1 Team) 2019 *Rev. Sci. Instrum.* **90** 043504
[27] Gradic D, Perseo V, König R and Ennis D *et al* 2019 *Fusion Eng. Des.* **146** 995–8
[28] Krychowiak M, König R, Klinger T and Fischer R 2004 *J. Appl. Phys.* **96** 4784–92
[29] Allcock J 2021 New techniques for coherence imaging fusion plasmas *PhD Thesis* Durham University